

WASSERSTEIN DISTORTION: UNIFYING FIDELITY AND REALISM

Yang QIU

School of Electrical and Computer Engineering
Cornell University
Ithaca, NY 14853 USA
yq268@cornell.edu

Aaron B. Wagner

School of Electrical and Computer Engineering
Cornell University
Ithaca, NY 14853 USA
wagner@cornell.edu

Johannes Ballé

Google Research
Mountain View, CA 94043 USA
jballe@google.com

Lucas Theis

Google Research
London, UK
theis@google.com

ABSTRACT

We introduce a distortion measure for images, *Wasserstein distortion*, that simultaneously generalizes pixel-level fidelity on the one hand and realism on the other. We show how Wasserstein distortion reduces mathematically to a pure fidelity constraint or a pure realism constraint under different parameter choices. Pairs of images that are close under Wasserstein distortion illustrate its utility. In particular, we generate random textures that have high fidelity to a reference texture in one location of the image and smoothly transition to an independent realization of the texture as one moves away from this point. Connections between Wasserstein distortion and models of the human visual system are noted.

1 INTRODUCTION

Classical image compression algorithms are optimized to achieve high pixel-level fidelity between the source and the reconstruction. That is, one views images as vectors in Euclidean space and seeks to minimize the distance between the original and reproduction using metrics such as PSNR, SSIM (Wang et al., 2004), etc. (Avcıbaşı et al., 2002; Dosselmann & Yang, 2005; Hore & Ziou, 2010). While effective to a large extent (Berger, 1971; Pearlman & Said, 2011; Sayood, 2017), these objectives have long been known to introduce artifacts, such as blurriness, into the reconstructed image (Wang & Bovik, 2009). Similar artifacts arise in image denoising (Buades et al., 2005), deblurring (Nah et al., 2021), and super-resolution (Kwon et al., 2015).

Recently, it has been observed that such artifacts can be reduced if one simultaneously maximizes the *realism*¹ of the reconstructed images. Specifically, one seeks to minimize the distance between some distribution induced by the reconstructed images and the corresponding distribution for natural images (Blau & Michaeli (2018); see also Delp & Mitchell (1991); Li et al. (2011); Saldi et al. (2014)). A reconstruction algorithm that ensures that these distributions are close will naturally be free of obvious artifacts; the two distributions cannot be close if one is supported on the space of crisp images and the other is supported on the space of blurry images. Image reconstruction under realism constraints has been a subject of intensive research of late, both of an experimental (Rippel & Bourdev, 2017; Tschannen et al., 2018; Agustsson et al., 2019; Mentzer et al., 2020) and theoretical (Klejsa et al., 2013; Blau & Michaeli, 2018; 2019; Matsumoto, 2018; 2019; Theis & Wagner, 2021; Chen et al., 2021; 2022; Wagner, 2022; Hamdi & Gündüz, 2023) nature.

Up to now, the dual objectives of fidelity and realism have been treated as distinct and even in tension (Blau & Michaeli, 2018; Zhang et al., 2021; Chen et al., 2022; Niu et al., 2023; Salehkalaibar et al., 2023). Yet they represent two attempts to capture the same notion, namely the differences perceived by a human observer. It is natural then to seek a simultaneous generalization of the two.

¹Realism is also referred to as *perceptual quality* by some authors.

Such a generalization could be more aligned with human perception than either objective alone, or even a linear combination of the two. The main contribution of this paper is one such generalization, *Wasserstein distortion*, which is grounded in models of the Human Visual System (HVS).

Realism objectives take several forms depending on how one induces a probability distribution from images. First, one can consider the distribution induced by the ensemble of full resolution images (Theis & Wagner, 2021; Theis et al., 2022; Wagner, 2022; Chen et al., 2022; Hamdi & Gündüz, 2023). Second, one can form a distribution over patches by selecting a patch at random from within a randomly selected image (Agustsson et al., 2019). Finally, for a given image, one can consider the distribution over patches induced by selecting a location at random and extracting the resulting patch (Wang et al., 2018; Gao et al., 2021). Theoretical studies have tended to focus on the first approach while experimental studies have focused more on patches. We shall focus on the third approach because it lends itself more naturally to unification with fidelity: both depend only on the image under examination without reference to other images in the ensemble. That said, the proposed Wasserstein distortion can be extended naturally to videos and other sequences of images and in this way it generalizes the other notions of realism. Under an ergodicity assumption, as occurs with textures, ensemble and per-image notions of realism coincide; see Corollary 3.4 to follow and the discussion in Portilla & Simoncelli (2000, p. 51).

Our simultaneous generalization of fidelity and realism is based in theories of the HVS, as noted above; namely it resorts to computing *summary statistics* in parts of the visual field where capacity is limited (Balas et al., 2009; Rosenholtz, 2011; Rosenholtz et al., 2012). In particular, Freeman & Simoncelli (2011) propose a model of the HVS focusing on the first two areas of the ventral stream, V1 and V2. The V1 responses are modeled as the outputs

of oriented filters spanning the visual field with different orientations and spatial frequencies. The second area computes higher order statistics from the V1 outputs over various receptive fields. The receptive fields grow with eccentricity, as depicted in Fig. 1. In the visual periphery, the receptive fields are large and only the response statistics pooled over a large area are acquired. In the fovea, i.e., the center of gaze, the receptive field is assumed small enough that the statistics uniquely determine the image itself. See Freeman & Simoncelli (2011) for a complete description of the model. One virtue of this model is that it does not require separate theories of foveal and peripheral vision: the distinction between the two is simply the result of different receptive field sizes.

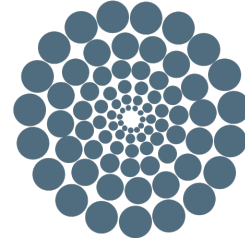


Figure 1: Receptive fields in the ventral stream grow with eccentricity.

This unification of foveal and peripheral vision likewise suggests a way of unifying fidelity and realism objectives. Similar to Freeman & Simoncelli (2011), we cover an image with overlapping pooling regions of various sizes. To each region we associate a distribution obtained by computing various features at random locations within the region. The overall distortion between two images is defined to be the Wasserstein distance between the distributions summed over the pooling regions, which we call *Wasserstein distortion*. We prove that as the receptive field size shrinks to zero, this distortion reduces to the underlying cost metric associated with the Wasserstein distance, recovering fidelity. As the receptive field size tends to infinity, we prove that the distortion captures the divergence in statistics between the two images without reference to the pixel values, recovering realism. Intermediate-sized pooling regions are also possible, and the sizes of the pooling regions can vary spatially over the image.

As a proof of concept, we generate random images that are close to a reference image under Wasserstein distortion. We find that if we use only large pooling regions, corresponding to a pure realism objective, we obtain texture reproductions that are competitive with dedicated texture generators. On the other hand, by using pooling regions of different sizes, we can create novel texture reproductions that have high fidelity to the reference in a designated location and smoothly transition to an independent realization of the texture as one moves away from this point. For more general images, we show how a saliency map can be used to automatically determine pooling regions. Then generating a random image that is close to the reference under Wasserstein distortion yields high-quality reproductions that are faithful to the original in regions of interest and realistic elsewhere.

The balance of the paper is organized as follows. Section 2 consists of a mathematical description of Wasserstein distortion. Section 3 shows the reduction to pure fidelity and pure realism as the size of the pooling region tends to zero and infinity, respectively. Section 4 contains our experimental results, primarily randomly generated images that are close to references under our distortion measure, along with some auxiliary experiments.

2 WASSERSTEIN DISTORTION

We now turn to defining Wasserstein distortion between a reference image, represented by a sequence $\mathbf{x} = \{x_n\}_{n=-\infty}^{\infty}$, and a reconstructed image, denoted by $\hat{\mathbf{x}} = \{\hat{x}_n\}_{n=-\infty}^{\infty}$. For notational simplicity, we shall consider 1-D sequences of infinite length, the 2-D case being a straightforward extension. Of course, any recorded image will have finite extents; with some care, we find that handling the boundaries in practice is not difficult, as demonstrated in Section 4.

Let T denote the unit advance operation, i.e., if $\mathbf{x}' = T\mathbf{x}$ then

$$x'_n = x_{n+1}. \quad (1)$$

We denote the k -fold composition $T \circ T \circ \dots \circ T$ by T^k . Let $\phi(\mathbf{x}) : \mathbb{R}^{\mathbb{Z}} \mapsto \mathbb{R}^d$ denote a vector of local features of $\{x_n\}_{n=-\infty}^{\infty}$ about $n = 0$. The simplest example is the coordinate map, $\phi(\mathbf{x}) = x_0$. More generally, $\phi(\cdot)$ can take the form of a convolution with a kernel $\alpha(\cdot)$

$$\phi(\mathbf{x}) = \sum_{k=-m}^m \alpha(k) \cdot x_k, \quad (2)$$

or, since ϕ may be vector-valued, it can take the form of a convolution with several kernels of the form in (2). Following Portilla & Simoncelli (2000) and Freeman & Simoncelli (2011), one could choose $\phi(\cdot)$ to be a steerable pyramid (Simoncelli & Freeman, 1995; see also Balas et al., 2009; Rosenholtz, 2011; Rosenholtz et al., 2012). Following Ustyuzhaninov et al. (2017), the components of ϕ could take the form of convolution with a kernel as in (2), with random weights, followed by a nonlinear activation function. More generally, $\phi(\cdot)$ can take the form of a trained multi-layer convolutional neural network, as in Gatys et al. (2015).

Define the sequence \mathbf{z} by

$$z_n = \phi(T^n \mathbf{x}) \quad (3)$$

and note that $z_n \in \mathbb{R}^d$ for each n . We view \mathbf{z} as a representation of the image \mathbf{x} in feature space.

Let $q_\sigma(k)$, $k \in \mathbb{Z}$, denote a family of probability mass functions (PMFs) over the integers, parameterized by $0 \leq \sigma < \infty$, satisfying:

- P.1** For any σ and k , $q_\sigma(k) = q_\sigma(-k)$;
- P.2** For any σ and $k, k' \in \mathbb{Z}$ such that $|k| \leq |k'|$, $q_\sigma(k) \geq q_\sigma(k')$;
- P.3** If $\sigma = 0$, q_σ is the Kronecker delta function, i.e., $q_0(k) = \begin{cases} 1 & k = 0 \\ 0 & k \neq 0 \end{cases}$;
- P.4** For all k , $q_\sigma(k)$ is continuous in σ at $\sigma = 0$;
- P.5** There exists $\epsilon > 0$ and K so that for all k such that $|k| \geq K$, $q_\sigma(k)$ is nondecreasing in σ over the range $[0, \epsilon]$; and
- P.6** For any k , $\lim_{\sigma \rightarrow \infty} q_\sigma(k) = 0$.

We call $q_\sigma(\cdot)$ the *pooling PMF* and σ the *pooling width* or *pooling parameter*. One PMF satisfying **P.1-P.6** is the two-sided geometric distribution,

$$q_\sigma(k) = \begin{cases} \frac{e^{1/\sigma}-1}{e^{1/\sigma}+1} \cdot e^{-|k|/\sigma} & \text{if } \sigma > 0 \\ 1 & \text{if } \sigma = 0 \text{ and } k = 0 \\ 0 & \text{otherwise.} \end{cases} \quad (4)$$

From the sequence \mathbf{x} , we define a sequence of probability measures $\mathbf{y}_\sigma = \{y_{n,\sigma}\}_{n=-\infty}^{\infty}$ via

$$y_{n,\sigma} = \sum_{k=-\infty}^{\infty} q_\sigma(k) \delta_{z_{n+k}}, \quad (5)$$

where \mathbf{z} is related to \mathbf{x} through (3) and $\delta \cdot$ denotes the Dirac delta measure. Each measure $y_{n,\sigma}$ in the sequence represents the statistics of the features pooled across a region centered at n with effective width σ . Note that all measures in \mathbf{y} share the same countable support set in \mathbb{R}^d ; they differ only in the probability that they assign to the points in this set. See Fig. 2.

Similarly, we can define $\hat{\mathbf{x}} = \{\hat{x}_n\}_{n=-\infty}^{\infty}$, $\hat{\mathbf{z}} = \{\hat{z}_n\}_{n=-\infty}^{\infty}$, and $\hat{\mathbf{y}}_\sigma = \{\hat{y}_{n,\sigma}\}_{n=-\infty}^{\infty}$ for the reconstructed image.

Let $d : \mathbb{R}^d \times \mathbb{R}^d \mapsto [0, \infty)$ denote an arbitrary distortion measure over the feature space. One natural choice is Euclidean distance

$$d(z, \hat{z}) = \|z - \hat{z}\|_2, \quad (6)$$

although in general we do not even assume that d is a metric. We define the distortion between the reference and reconstructed images at location n to be

$$D_{n,\sigma} = W_p^p(y_{n,\sigma}, \hat{y}_{n,\sigma}), \quad (7)$$

where W_p denotes the Wasserstein distance of order p (Villani, 2009, Def. 6.1)²:

$$W_p(\rho, \hat{\rho}) = \inf_{Z \sim \rho, \hat{Z} \sim \hat{\rho}} \mathbb{E} \left[d^p(Z, \hat{Z}) \right]^{1/p}, \quad (8)$$

where ρ and $\hat{\rho}$ are probability measures on \mathbb{R}^d . The distortion over a block $\{-N, \dots, N\}$ (such as a full image) is defined as the spatial average

$$D = \frac{1}{2N+1} \sum_{n=-N}^N D_{n,\sigma}. \quad (9)$$

This assumes that the pooling parameter, σ , is the same for all n . In practice, it is desirable to vary the size of the pooling regions across the image. One can easily extend the above definition to allow σ to depend on n :

$$D = \frac{1}{2N+1} \sum_{n=-N}^N D_{n,\sigma(n)} \quad (10)$$

$$= \frac{1}{2N+1} \sum_{n=-N}^N W_p^p(y_{n,\sigma(n)}, \hat{y}_{n,\sigma(n)}). \quad (11)$$

We call the function $\sigma(\cdot)$ the σ -map.

Wasserstein distance is widely employed due to its favorable theoretical properties, and indeed our theoretical results use the Wasserstein distance in (8) for some p and d . In practice one might adopt a proxy for (8) that is easier to compute. Following the approach used with Fréchet Inception Distance (FID) (Heusel et al., 2017; Lucic et al., 2018; Liu et al., 2020; Fan et al., 2022), one could replace (8) with

$$\|\mu - \hat{\mu}\|_2^2 + \text{Tr}(C + \hat{C} - 2(\hat{C}^{1/2} C \hat{C}^{1/2})^{1/2}). \quad (12)$$

This is equivalent to W_p^p if we take $p = 2$, d to be Euclidean distance, and assume that ρ (resp. $\hat{\rho}$) is Gaussian with mean μ (resp. $\hat{\mu}$) and covariance matrix C (resp. \hat{C}) (Olkin & Pukelsheim, 1982). In our experiments, we simplify this even further by assuming that the features are uncorrelated,

$$\sum_{i=1}^d (\mu_i - \hat{\mu}_i)^2 + \left(\sqrt{V_i} - \sqrt{\hat{V}_i} \right)^2, \quad (13)$$

where μ_i and V_i are the mean and variance of the i th component under ρ and similarly for $\hat{\rho}$. This is justified when the feature set is overcomplete because the correlation between two features is likely to be captured by some third feature. Other possible proxies include sliced Wasserstein distance (Pitié et al., 2005; Bonneel et al., 2015; Tartavel et al., 2016; Heitz et al., 2021), Sinkhorn distance (Cuturi, 2013), Maximum Mean Discrepancy (MMD) (Smola et al., 2006; Li et al., 2017; 2019), or the distance between Gram matrices (Gatys et al., 2015; Ustyuzhaninov et al., 2017).

²We refer to W_p as the Wasserstein *distance* even though it is not necessarily a metric if d is not a metric.

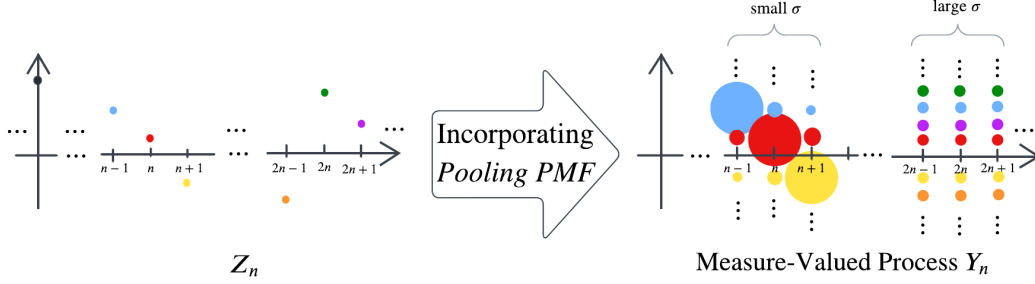


Figure 2: A pictorial illustration of (5). In the right plot, the size of the disk indicates the probability mass and the vertical coordinate of the center of the disk indicates the value.

The idea of measuring the discrepancy between images via the Wasserstein distance, or some proxy thereof, between distributions in feature space is not new (Rubner et al., 2000; Pitié et al., 2005; Tartavel et al., 2016; Heitz et al., 2021; Elnekave & Weiss, 2022; Houdard et al., 2023). Past applications of this idea have considered empirical distributions with equal weights over the pixels. The primary contribution of this paper is to note that using nonuniform weights over pixels (compare (5) with, e.g., Eq. (1) of Heitz et al. (2021)) is supported by models of the HVS and allows us to lift fidelity and realism into a common framework.

3 FIDELITY AND REALISM AS EXTREME CASES

Let \mathbf{x} and $\hat{\mathbf{x}}$ be two sequences and let \mathbf{z} and $\hat{\mathbf{z}}$ denote the associated feature sequences, i.e., $z_n = \phi(T^n \mathbf{x})$ and $\hat{z}_n = \phi(T^n \hat{\mathbf{x}})$. If one is only concerned with fidelity to the original image, one might use an objective such as

$$\frac{1}{2N+1} \sum_{n=-N}^N d^p(z_n, \hat{z}_n), \quad (14)$$

perhaps with ϕ being the identity map; conventional mean squared error can be expressed in this way. This objective can be trivially recovered from Wasserstein distortion by taking $\sigma = 0$, invoking **P.3**, and applying the formula for the Wasserstein distance between point masses:

$$W_p(\delta_z, \delta_{\hat{z}}) = d(z, \hat{z}). \quad (15)$$

Given that we are interested in smoothly interpolating between fidelity and realism, we would like Wasserstein distortion to reduce to (14) in the limit as $\sigma \rightarrow 0$. We next identify conditions under which this continuity result holds. Note that this result does not require d to be a metric.

Theorem 3.1. *Suppose q satisfies **P.3** – **P.5** and \mathbf{z} , $\hat{\mathbf{z}}$, and q together satisfy*

$$\sum_{k=-\infty}^{\infty} q_{\sigma}(k) d^p(z_k, \hat{z}_k) < \infty \quad (16)$$

for all $\sigma > 0$. Then we have

$$\lim_{\sigma \rightarrow 0} D_{0,\sigma} = d^p(z_0, \hat{z}_0). \quad (17)$$

We first prove a lemma.

Lemma 3.2 (Equivalence of Cesàro Sums). *Suppose q satisfies **P.1**, **P.2**, and **P.6**. For any two-sided \mathbb{R} -valued sequence \mathbf{a} , if*

$$\lim_{m \rightarrow \infty} \frac{1}{2m+1} \sum_{k=-m}^m a_k = \alpha \in \mathbb{R}, \quad (18)$$

and for all $\sigma > 0$,

$$\sum_{k=-\infty}^{\infty} q_{\sigma}(k) |a_k| < \infty, \quad (19)$$

then we likewise have

$$\lim_{\sigma \rightarrow \infty} \sum_{k=-\infty}^{\infty} q_{\sigma}(k) a_k = \alpha. \quad (20)$$

Proof. We can write

$$\sum_{\ell=-\infty}^{\infty} q_{\sigma}(\ell) a_{\ell} = \lim_{k \rightarrow \infty} \sum_{\ell=-(k-1)}^{k-1} (q_{\sigma}(\ell) - q_{\sigma}(k)) a_{\ell} \quad (21)$$

$$= \lim_{k \rightarrow \infty} \sum_{\ell=-(k-1)}^{k-1} \sum_{m=|\ell|}^{k-1} (q_{\sigma}(m) - q_{\sigma}(m+1)) a_{\ell} \quad (22)$$

$$= \lim_{k \rightarrow \infty} \sum_{m=0}^{k-1} \sum_{\ell=-m}^m (q_{\sigma}(m) - q_{\sigma}(m+1)) a_{\ell} \quad (23)$$

$$= \sum_{m=0}^{\infty} \sum_{\ell=-m}^m (q_{\sigma}(m) - q_{\sigma}(m+1)) a_{\ell}, \quad (24)$$

where (21) holds by (19), **(P.1)**, **(P.2)**, and dominated convergence. For $m \geq 0$, define the sequences

$$b_m = \frac{1}{2m+1} \sum_{\ell=-m}^m a_{\ell} \quad (25)$$

and

$$r_{\sigma}(m) = (q_{\sigma}(m) - q_{\sigma}(m+1)) (2m+1). \quad (26)$$

By **(P.2)**, $r_{\sigma}(m) \geq 0$. By (24),

$$\sum_{\ell=-\infty}^{\infty} q_{\sigma}(\ell) a_{\ell} = \sum_{m=0}^{\infty} r_{\sigma}(m) b_m. \quad (27)$$

Now the choice $a_{\ell} = 1$ satisfies (19) and in this case the previous equation reads $\sum_{m=0}^{\infty} r_{\sigma}(m) = 1$. Fix $\epsilon > 0$ and M such that for all $m > M$, $|b_m - \alpha| < \epsilon$. We can write

$$\left| \sum_{\ell=-\infty}^{\infty} q_{\sigma}(\ell) a_{\ell} - \alpha \right| \leq \left| \sum_{m=0}^M r_{\sigma}(m) (b_m - \alpha) \right| + \left| \sum_{m=M+1}^{\infty} r_{\sigma}(m) (b_m - \alpha) \right| \quad (28)$$

$$\leq \left(\sum_{m=0}^M r_{\sigma}(m) \right) \left(\max_{m=0,1,\dots,M} b_m + |\alpha| \right) + \epsilon. \quad (29)$$

Taking $\sigma \rightarrow \infty$ on both sides, the conclusion follows by **P.6**. \square

Proof of Theorem 3.1. Fix K and ϵ as in **P.5**. Consider the coupling between $y_{0,\sigma}$ and $\hat{y}_{0,\sigma}$ suggested by the ordering of the sequences:

$$D_{0,\sigma} = \inf_{Z \sim y_{n,\sigma}, \hat{Z} \sim \hat{y}_{n,\sigma}} E[d^p(Z, \hat{Z})] \leq \sum_{k=-\infty}^{\infty} q_{\sigma}(k) d^p(z_k, \hat{z}_k). \quad (30)$$

We have

$$\limsup_{\sigma \rightarrow 0} D_{0,\sigma} \leq \lim_{\sigma \rightarrow 0} q_{\sigma}(0) d^p(z_0, \hat{z}_0) + \lim_{\sigma \rightarrow 0} \sum_{k: 0 < |k| \leq K} q_{\sigma}(k) d^p(z_k, \hat{z}_k) \quad (31)$$

$$\begin{aligned} &+ \lim_{\sigma \rightarrow 0} \sum_{k: |k| > K} q_{\sigma}(k) d^p(z_k, \hat{z}_k) \\ &= d^p(z_0, \hat{z}_0), \end{aligned} \quad (32)$$

where (32) follows from **P.3** and **P.4** (for the first two limits) and from **P.3-P.5** and dominated convergence (for the third limit). For the reverse direction, fix $\sigma > 0$ and let $q_\sigma(\cdot, \cdot)$ denote any PMF over \mathbb{Z}^2 , both of whose marginals are $q_\sigma(\cdot)$. Then we have

$$\sum_{k_1=-\infty}^{\infty} \sum_{k_2=-\infty}^{\infty} q_\sigma(k_1, k_2) d^p(z_{k_1}, \hat{z}_{k_2}) \geq q_\sigma(0, 0) d^p(z_0, \hat{z}_0) \quad (33)$$

$$\geq (2q_\sigma(0) - 1) d^p(z_0, \hat{z}_0), \quad (34)$$

from which the result follows by **P.3** and **P.4**. \square

Likewise, we show that Wasserstein distortion continuously reduces to pure realism in the large- σ limit. We use \xrightarrow{w} to denote weak convergence.

Theorem 3.3. *Suppose q satisfies **P.1**, **P.2**, and **P.6** and d is a metric. Let F_N (resp. \hat{F}_N) denote the empirical CDF of $\{z_{-N}, \dots, z_N\}$ (resp. $\{\hat{z}_{-N}, \dots, \hat{z}_N\}$) and suppose we have*

$$F_N \xrightarrow{w} F \text{ and } \hat{F}_N \xrightarrow{w} \hat{F} \quad (35)$$

$$\int d^p(z, 0) dF_N \rightarrow \int d^p(z, 0) dF < \infty \text{ and } \int d^p(z, 0) d\hat{F}_N \rightarrow \int d^p(z, 0) d\hat{F} < \infty \quad (36)$$

and, for all σ ,

$$\sum_{k=-\infty}^{\infty} q_\sigma(k) d^p(z_k, 0) < \infty \text{ and } \sum_{k=-\infty}^{\infty} q_\sigma(k) d^p(\hat{z}_k, 0) < \infty. \quad (37)$$

Then we have

$$\lim_{\sigma \rightarrow \infty} D_{0, \sigma} = W_p^p(F, \hat{F}). \quad (38)$$

Proof. With a slight abuse of notation we let F_σ denote the CDF of the distribution

$$\sum_{k=-\infty}^{\infty} q_\sigma(k) \delta_{z_k} \quad (39)$$

and define \hat{F}_σ analogously. Then $D_{0, \sigma} = W_p^p(F_\sigma, \hat{F}_\sigma)$. By the triangle inequality for Wasserstein distance (Villani, 2009, p. 94) (which requires d to be a metric),

$$W_p(F_\sigma, \hat{F}_\sigma) \leq W_p(F_\sigma, F) + W_p(F, \hat{F}) + W_p(\hat{F}, \hat{F}_\sigma). \quad (40)$$

By Lemma 3.2 and (35), $F_\sigma \xrightarrow{w} F$. By Lemma 3.2, (36), and (37), we have

$$\lim_{\sigma \rightarrow \infty} \int d^p(z, 0) dF_\sigma(z) = \int d^p(z, 0) dF(z). \quad (41)$$

These two conditions imply that $W_p(F_\sigma, F) \rightarrow 0$ as $\sigma \rightarrow \infty$ (Villani, 2009, Thm. 6.9). Similarly we have $W_p(\hat{F}, \hat{F}_\sigma) \rightarrow 0$, yielding

$$\limsup_{\sigma \rightarrow \infty} D_{0, \sigma} \leq W_p^p(F, \hat{F}). \quad (42)$$

Applying the triangle inequality in the reverse direction gives

$$W_p(F, \hat{F}) \leq W_p(F, F_\sigma) + W_p(F_\sigma, \hat{F}_\sigma) + W_p(\hat{F}_\sigma, \hat{F}). \quad (43)$$

Taking limits yields

$$\liminf_{\sigma \rightarrow \infty} D_{0, \sigma} \geq W_p^p(F, \hat{F}) \quad (44)$$

and the theorem. \square

It follows from the previous result that when the source ensemble is ergodic, as occurs with textures, then in the large- σ limit Wasserstein distortion reduces to the ensemble form of realism. That is, it equals the Wasserstein distance (to the p th power) between the true distributions of the images and reconstructions, denoted by F and \hat{F} in the following corollary.

Corollary 3.4. Suppose q satisfies **P.1**, **P.2**, and **P.6** and d is a metric. Suppose \mathbf{X} and $\hat{\mathbf{X}}$ are stationary ergodic processes and let F (resp. \hat{F}) denote the CDF of Z_0 (resp. \hat{Z}_0). If

$$\mathbb{E}[d^p(Z_0, 0)] < \infty \text{ and } \mathbb{E}[d^p(\hat{Z}_0, 0)] < \infty, \quad (45)$$

then we have

$$\lim_{\sigma \rightarrow \infty} D_{0,\sigma} = W_p^p(F, \hat{F}) \quad a.s. \quad (46)$$

Proof. Among the hypotheses of Theorem 3.3, (35) and (36) hold a.s. by the ergodic theorem (e.g., Durrett (1996, Thm 6.2.1)) and (45), and (37) holds a.s. because

$$\mathbb{E} \left[\sum_{k=-\infty}^{\infty} q_{\sigma}(k) d^p(Z_k, 0) \right] = \sum_{k=-\infty}^{\infty} q_{\sigma}(k) \mathbb{E}[d^p(Z_k, 0)] = \mathbb{E}[d^p(Z_0, 0)] < \infty, \quad (47)$$

by monotone convergence and (45), and similarly for \hat{Z} . \square

4 EXPERIMENTS

As a proof of concept, we consider the use of Wasserstein distortion to generate random images that resemble a given reference image. Specifically, we take an image of random pixels and iteratively modify it to reduce its Wasserstein distortion to the original. Following Gatys et al. (2015), we use as our feature map selected activations within the VGG-19 network, with some modifications. The following Section 4.1 provides a detailed description of VGG-19 and our modifications; here we note only that we augment the VGG-19 features to include the raw pixel values. We found that including this “0th” layer of the network provides for an improved reproduction of the DC level of the image. We use the scalar Gaussianized Wasserstein distance in (13) as a computational proxy for (8). For the pooling PMF, we take the horizontal and vertical offsets to be i.i.d. according to the two-sided geometric distribution, conditioned on landing within the boundaries of the image. It should be emphasized that our framework is agnostic to the choice of the feature map, the distance proxy, and the pooling PMF.

The Wasserstein distortion is defined at every location in the image. This is entirely analogous to the way that the squared error between images is defined at every location. In our case, computation limitations prevent us from evaluating the distortion at every location in images of a reasonable size unless σ is small. In parts of the image in which σ is large, we found that satisfactory results could be obtained by evaluating the distortion at a subset of points, with the subset randomly selected between iterations. When $\sigma = 0$, Wasserstein distortion reduces to MSE, and in this case, we skip the computation of the variance in (13), since it must be zero. This affords some reduction in computation, which allows us to evaluate the distortion at a larger set of points.

We minimize the Wasserstein distortion between the reference and reconstructed images using the L-BFGS algorithm (Zhu et al., 1997) with 4,000 iterations and an early stopping criterion.

4.1 EXPERIMENTAL SETUP

Our work utilizes the VGG-19 network, although we emphasize that the framework is agnostic to the choice of features. Details of the VGG-19 network can be found in Simonyan & Zisserman (2015); we use the activation of selected layers as our features, with the following changes to the network structure:

1. All pooling layers in the original network in Simonyan & Zisserman (2015) use MaxPool; as suggested by Gatys et al. (2015), in our experiments we use AvePool;
2. There are 3 fully connected layers and a soft-max layer at the end in the original structure in Simonyan & Zisserman (2015), which we do not use;
3. We use the weights pre-trained on ImageNet (Deng et al., 2009), that are normalized such that over the validation set of ImageNet, the average activation of each layer is 1, as suggested in Gatys et al. (2015).

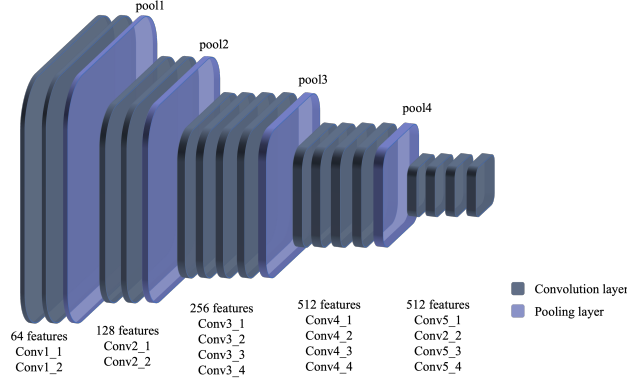


Figure 3: VGG-19 network structure.

Fig. 3 provides a illustration.

For all our experiments, the Wasserstein distortion is calculated as follows: we pass the pre-processed source image \mathbf{x} and reconstruction image $\hat{\mathbf{x}}$ through the VGG-19 network, and denote the response activation of each layer ℓ by \mathbf{z}^ℓ and $\hat{\mathbf{z}}^\ell$, respectively. We denote the source and reconstruction image themselves as the 0th layer. In pre-processing, we do not remove the DC component of the image, in contrast to the training process of VGG-19 network. For each experiment, we specify

1. a set of layers of interest;
2. for each spatial dimension, a method to compute the σ -map;
3. a method to determine the pixel of interest;
4. a multiplier M_ℓ and M_σ for each layer ℓ and each σ , respectively.

The activation response of all layers of interest (with activation being the identity map for 0-th layer if it is one layer of interest) can be seen as the feature $\phi(\mathbf{x})$ in our construction. For each layer of interest ℓ , we obtain the sequences of probability measures \mathbf{y}^ℓ and $\hat{\mathbf{y}}^\ell$ from \mathbf{z}^ℓ and $\hat{\mathbf{z}}^\ell$; for each pixel of interest $(i, j)^\ell$ in layer ℓ , we calculate the Wasserstein distortion $D_{i,j,\sigma}^\ell(y_{i,j,\sigma}^\ell, \hat{y}_{i,j,\sigma}^\ell) \times M_\sigma \times M_\ell$ with (13), where the σ is determined by the σ -map. The loss is

$$D = \sum_{\ell} \sum_{(i,j)^\ell} D_{i,j,\sigma}^\ell(y_{i,j,\sigma}^\ell, \hat{y}_{i,j,\sigma}^\ell) \times M_\sigma \times M_\ell. \quad (48)$$

For the first experiment, we use all layers up to (but excluding) the 4th pooling layer (pool4 in Fig. 3), and the weight is the inverse of the normalization factor; effectively raw ImageNet weights are applied.

For the second experiment, we use all layers up to (but excluding) the 4th pooling layer (pool4 in Fig. 3). For each layer, we evaluate the distortion at all high fidelity ($\sigma = 0$) pixels and 25 randomly chosen pixels that are not high fidelity pixels. We randomly choose 20 sets of 25 pixels, and randomly use one of the sets in each distortion calculation. For the 0th layer, $M_{\ell=0} = 100$; for the first 1/3 layers, $M_\ell = 10$; for the middle 1/3 layers, $M_\ell = 5$; and for the last 1/3 layers, $M_\ell = 1$. $M_{\sigma=0} = 1$ and $M_{\sigma \neq 0} = 200$.

The setup for the third experiment differs from the second only in the choice of σ map. From the given saliency map, we obtain a “saliency value” for each pixel, normalized to $[0, 1]$. All pixels with saliency value higher than the threshold of 0.1 are declared high saliency. The σ values for the remaining locations are determined using the procedure described in the main text.

4.2 EXPERIMENT 1: INDEPENDENT TEXTURE SYNTHESIS

We first consider the problem of generating an independent realization of a given texture (Portilla & Simoncelli, 2000; Gatys et al., 2015; Ustyuzhaninov et al., 2017; Heitz et al., 2021). We evaluate

the Wasserstein distortion at a single point in the center of the image with $\sigma = 4,000$. Since the images are 256x256 or 512x512, the Wasserstein distortion effectively acts as a realism objective, per Theorem 3.3.

The results are shown in the first two columns of Fig. 4 and Fig. 5. The results are commensurate with dedicated texture synthesis schemes (Gatys et al., 2015; Ustyuzhaninov et al., 2017; Heitz et al., 2021), which is unsurprising since with this σ -map, our setup is close to that of Heitz et al. (2021). The primary difference is that we use the 1-D Gaussianized Wasserstein distance in (13) in place of the sliced Wasserstein distance, which affords some computational savings. If there are d features within a layer and N pixels, the complexity of the scalar Gaussianized Wasserstein distance is dN compared with $d^2N + dN \log N$ for sliced Wasserstein distance (assuming d random projections, as is done in Heitz et al. (2021)). In practice, we find that this translates to a speedup of about 2x, with comparable quality on the textures of interest. We conclude that, at least with VGG-19 and the textures considered here, it is unnecessary to compute the full 1-D Wasserstein distance along random directions; comparing the first two moments along the coordinate axes is sufficient.

4.3 EXPERIMENT 2: PINNED TEXTURE SYNTHESIS

The power of Wasserstein distortion is that it can smoothly interpolate between fidelity and realism. We illustrate this with a variation of the first experiment in which σ varies spatially over the image. Specifically, we set $\sigma = 0$ for pixels near the center; other pixels are assigned a σ proportional to their distance to the nearest pixel with $\sigma = 0$, with the proportionality constant chosen so that the outermost pixels have a σ that is comparable to the width of the image. The choice of having σ grow linearly with distance to region of interest is supported by studies of the HVS, as described more fully in the next section. Under this σ -map, Wasserstein distortion behaves like a fidelity measure in the center of the image and a realism measure along the edges, with an interpolation of the two in between. The results are shown in the third and fourth columns in Fig. 4 and Fig. 5. The $\sigma = 0$ points have the effect of pinning the reconstruction to the original in the center, with a gradual transition to an independent realization at the edge.

4.4 EXPERIMENT 3: REPRODUCTION OF NATURAL IMAGES WITH SALIENCY MAPS

We turn to the reproduction of natural images. We use the SALICON dataset (Jiang et al., 2015) which provides a saliency map for each image that we use to produce a σ -map. Specifically, we set a saliency threshold above which points are declared to be high salience. For such points we set $\sigma = 0$. For all other points σ is proportional to the distance to the nearest high-saliency point, with the proportionality constant determined by the constraint that the farthest points should have a σ value on par with the width of the image.

The choice of having σ grow linearly with distance from the high saliency region is supported by studies of the HVS. There is both physiological (Dumoulin & Wandell, 2008) and operational (Freeman & Simoncelli, 2011) evidence that the size of the receptive fields in the HVS grows linearly with eccentricity. If one seeks to produce images that are difficult for a human observer to easily distinguish, it is natural to match the pooling regions to the corresponding receptive fields when the gaze is focused on the high saliency region.

The results are shown in Fig. 6 and Fig. 7. For images for which the non-salient regions are primarily textures, the reproductions are plausible replacements for the originals. In some other cases, the images appear to be plausible replacements if one focuses on high saliency regions, but not if one scrutinizes the entire image. This suggests that Wasserstein distortion can capture the discrepancy observed by a human viewer focused on high-saliency regions.

It should be emphasized that the process of producing the reconstructions in Figs. 6 and 7 requires no pre-processing or manual labeling. In particular, it is not necessary to segment the image. Given a binarized saliency map, the σ -map can be constructed automatically using the above procedure, at which point the Wasserstein distortion is well defined and training can begin. It is possible that improved results could be obtained with a more sophisticated σ map, however. One intriguing possibility is to construct a σ map by combining a saliency map, estimates of receptive field sizes in the HVS, and a predicted viewing distance. It is believed that pooling actually occurs in some form at various levels of the HVS (Freeman & Simoncelli, 2011) and that receptive fields grow more

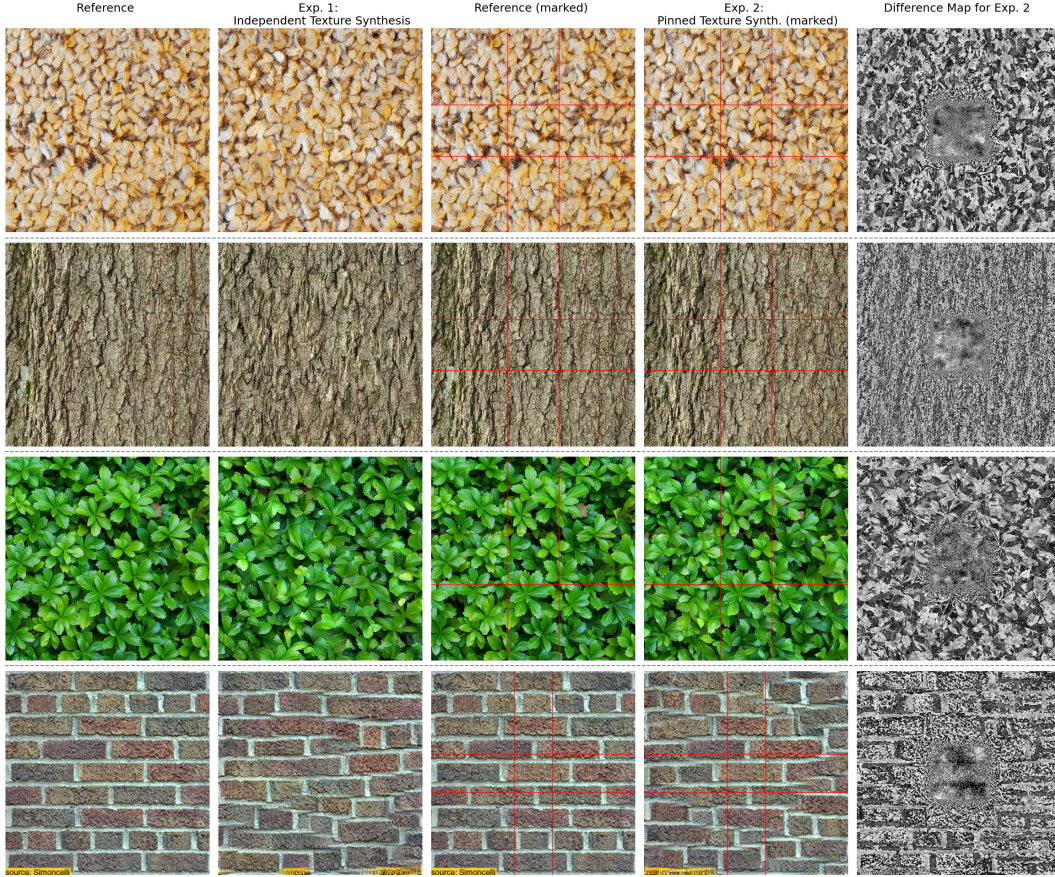


Figure 4: For each row, the first image is the reference texture; the second image is the reproduction texture under Experiment 1; the third and fourth images are the reference-reproduction pair under Experiment 2, with auxiliary lines drawn indicates the $\sigma = 0$ points; the fifth image is the difference of reference and reproduction textures under Experiment 2. For Experiment 1, the results are commensurate with dedicated texture generators. For Experiment 2, the reconstructions smoothly transition from pixel-level fidelity at the center to realism at the edges. See Fig. 5 for more examples.

quickly with eccentricity at higher levels. In the context of VGG-19, this suggests that it could be advantageous to use different σ -maps for different layers, with deeper layers having σ -values that grow more rapidly with distance from the high saliency region. How to optimize the σ -map, and in particular how to vary it across features, is an interesting direction for future work.

The next three auxiliary experiments illustrate certain properties of the Wasserstein distortion.

4.5 SEPARATE FIDELITY AND REALISM CONSTRAINTS ARE INSUFFICIENT

We illustrate that a linear combination of MSE distortion and Gram matrix distortion as defined in Gatys et al. (2015); Ustyuzhaninov et al. (2017), cannot achieve the reconstruction obtained through Wasserstein distortion. We calculate the MSE distortion over the high saliency area defined in Section 4.4, the Gram matrix distortion over the whole image as defined in Gatys et al. (2015); Ustyuzhaninov et al. (2017), and linearly combine the two with a multiplier on the Gram matrix distortion. Fig. 8 exhibits the results.

4.6 σ -PROGRESSION

We consider a variation of the experiment in Section 4.2: the pixels of interest is now a sparse and even grid of each spatial dimension; the sparse grid consists of no more than 255 pixels, and is no

finer than every 8 pixels. The σ map assigns the same σ to all pixels, and the σ value is varied for each experiment. Fig. 9 exhibits the reproductions for different σ values.

4.7 WASSERSTEIN DISTORTION VALUES FOR TEXTURES

Unless σ is small, we do not expect the Wasserstein distortion between images to be low if and only if the images are identical. Rather, it should be small if and only if the perceptual differences between the two are minor. To validate this hypothesis, we calculate the Wasserstein distortion between all possible pairs of images from Experiment 1 and Experiment 2. Results are shown in Fig. 10. All pixels are assigned $\sigma = 4,000$, with 9 pixels of interest that forms an even grid. Using (13) as the distortion measure, so long as the σ maps and sets of pixels of interest are compatible, we can compute the Wasserstein distortion between two images even they have different resolutions. We see that the distortion is small for images of the same texture and large for images that represent different textures.

5 DISCUSSION

Wasserstein distortion exploits a particularity of the HVS, which is its unique (among the various senses) ability to foveate, and hence extract information preferentially from spatial locations selected by gaze. It accomplishes this by interpolating between fidelity and realism, enabling results such as those in Experiments 2 and 3 (see also the σ -progression experiment, Section 4.6 for a different experiment illustrating the interpolation). Section 4.5 shows that a naive application of separate fidelity and realism objectives is insufficient to reproduce our results on natural images. It is possible that these results can be reproduced with a more clever application of the two objectives; one can never rule out such a possibility. In any event, viewing fidelity and realism as special cases of a more general objective is valuable from a purely conceptual standpoint.

The concept of realism as a divergence across ensembles of full-resolution images is at odds with the everyday observation that humans can distinguish realistic from unrealistic images by looking at a single example. Wasserstein distortion offers one possible explanation for *how* humans might make these one-shot judgements, namely by measuring realism across spatial regions. As demonstrated in the previous section, spatial realism may play a crucial role in modeling human perception, in particular in the visual periphery; and hence, for all practical applications, in regions of low saliency.

We have considered image generation as a proof of concept. The application of Wasserstein distortion to compression is natural and as yet unexplored. Practical image compressors optimized for Wasserstein distortion could encode statistics over pooling regions that vary in size depending on the distance from the salient parts of the image. Note that this approach would be distinct from only encoding high-saliency regions and using a generative model optimized for ensemble realism to “fill in” the remainder. The latter approach would rely on knowledge of the conditional distribution given the encoding rather than the local image statistics. As such, it would be allowed to deviate more significantly from the source image, so long as low-saliency regions that it creates are contextually plausible. It would also abruptly toggle from a focus on fidelity to a focus on realism as one moves away from high saliency areas. Theoretical characterizations of optimal compression schemes under Wasserstein distortion, along the lines of the rate-distortion-perception function (Blau & Michaeli, 2019; Theis & Wagner, 2021; Zhang et al., 2021; Chen et al., 2022; Wagner, 2022; Hamdi & Gündüz, 2023), are also of interest.

ACKNOWLEDGMENTS

The authors wish to thank Eiríkur Agustsson for calling their attention to Heitz et al. (2021). The first two authors were supported by the US National Science Foundation under grant CCF-2306278 and a gift from Google.

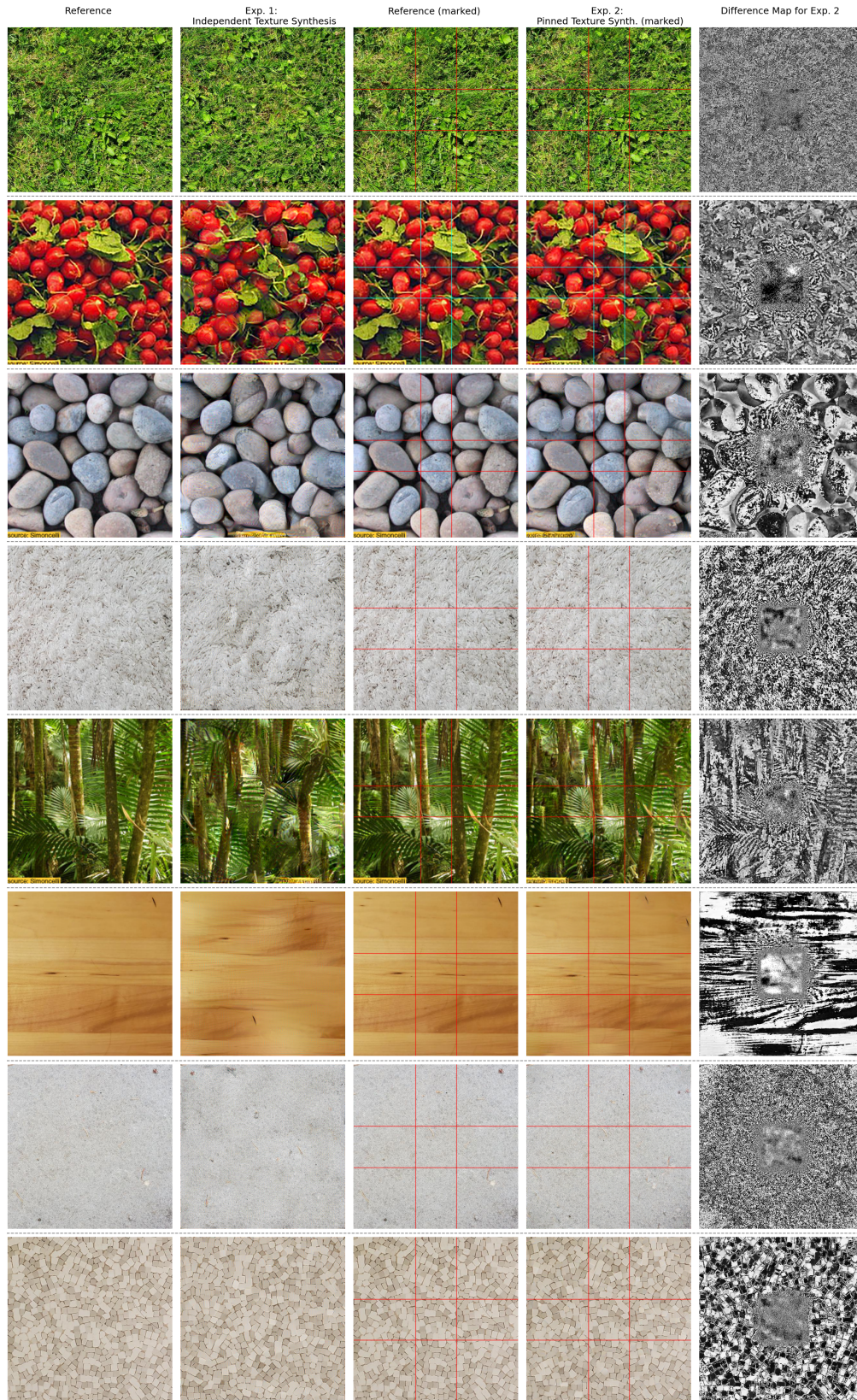


Figure 5: An extension of Fig. 4, consisting of more examples from Experiments 1 and 2.

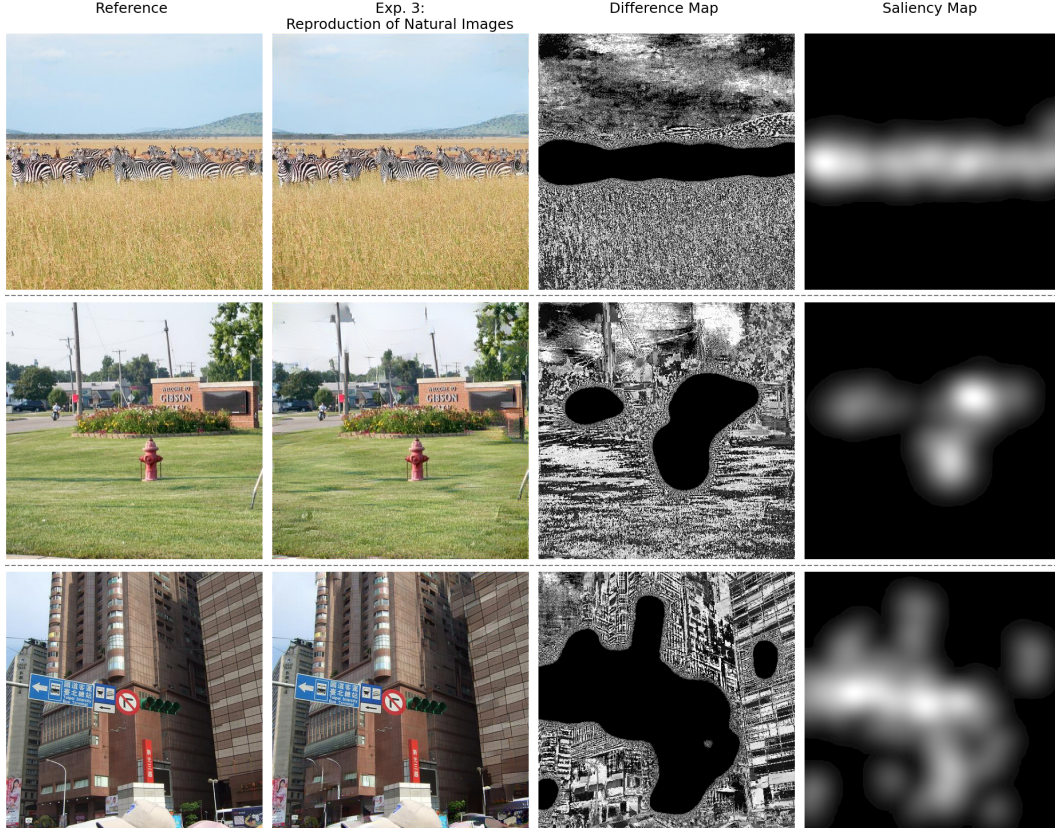


Figure 6: For each row, the first image is the reference image and the second is the reproduction; the third is the difference between the two; and the fourth is the saliency map from SALICON before binarization. In the high saliency regions, the reconstruction exhibits pixel-level fidelity. Elsewhere, it exhibits realism or an interpolation of the two. When focusing on high saliency regions, the images can be difficult to distinguish, but differences emerge upon inspection of the non-salient regions. Compare with Freeman & Simoncelli (2011, Fig. 2); see Fig. 7 for additional examples.

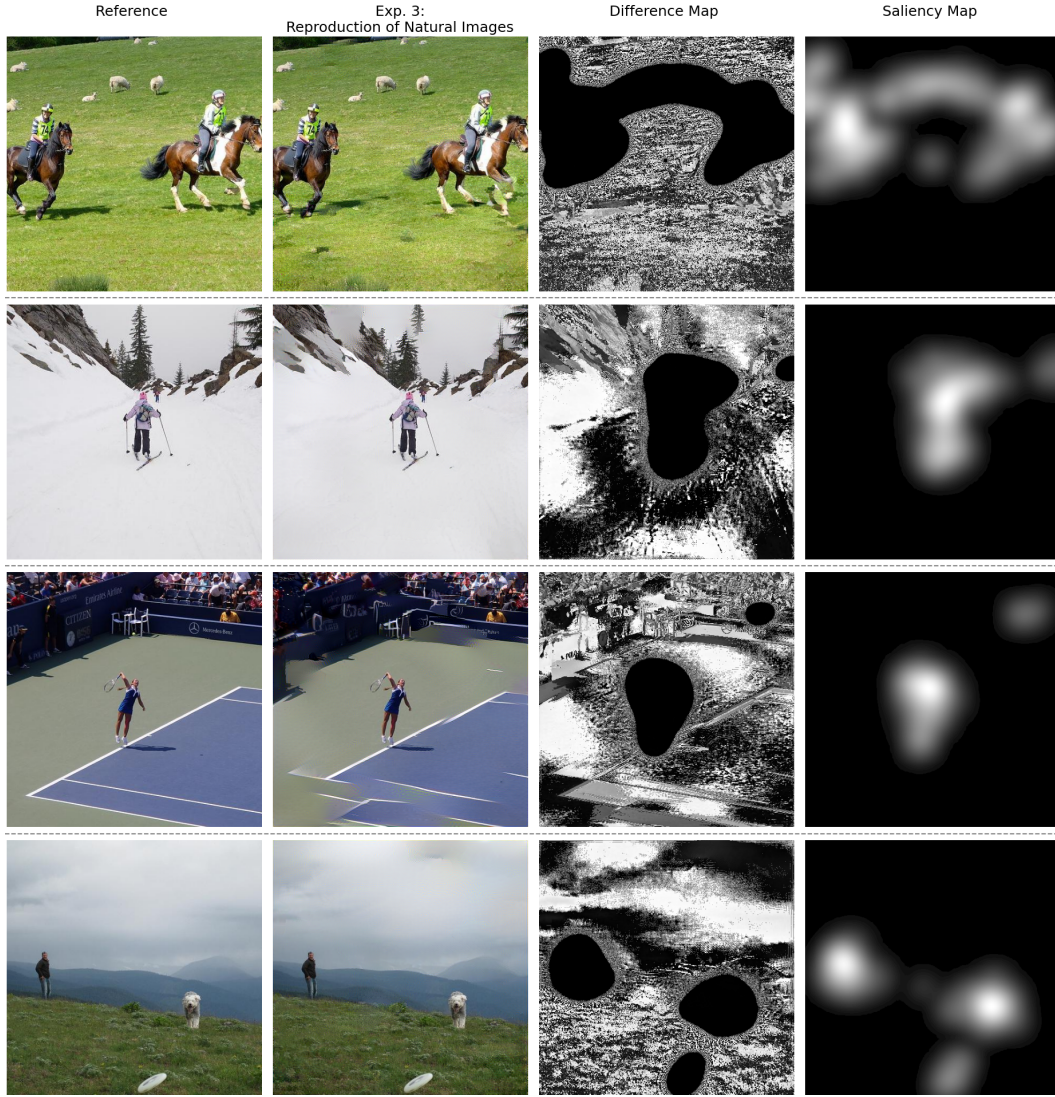


Figure 7: An extension of Fig. 6, consisting of more examples from Experiment 3. The misplaced foul lines in the third example are likely a manifestation of VGG-19’s recognized difficulty with reproducing long linear features in textures (Liu et al., 2016; Snelgrove, 2017; Sendik & Cohen-Or, 2017; Zhou et al., 2018; Gonthier et al., 2022).



Figure 8: The first two images are the reference image and its saliency map; the rest are reproductions, with different multipliers applied to the Gram matrix distortion in the linear combination.

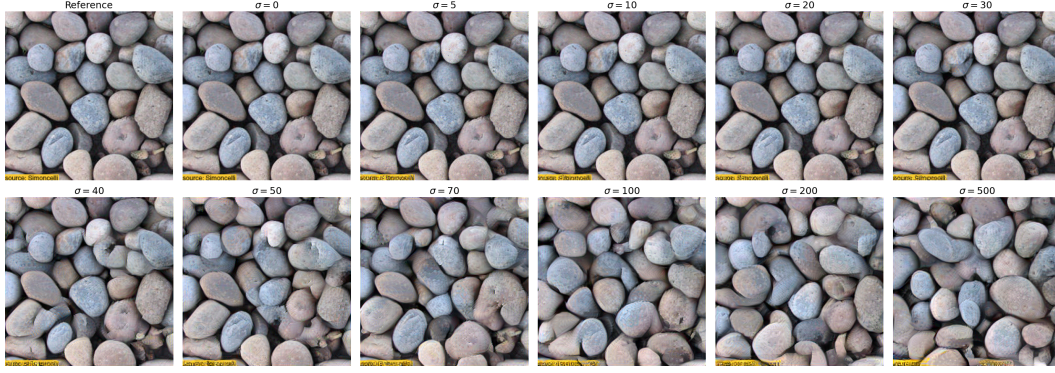


Figure 9: The first image is the reference; all others are reproductions under different σ 's. We see as σ increases, the generated image transitions from a pixel-accurate reproduction to an independent realization of the same texture.

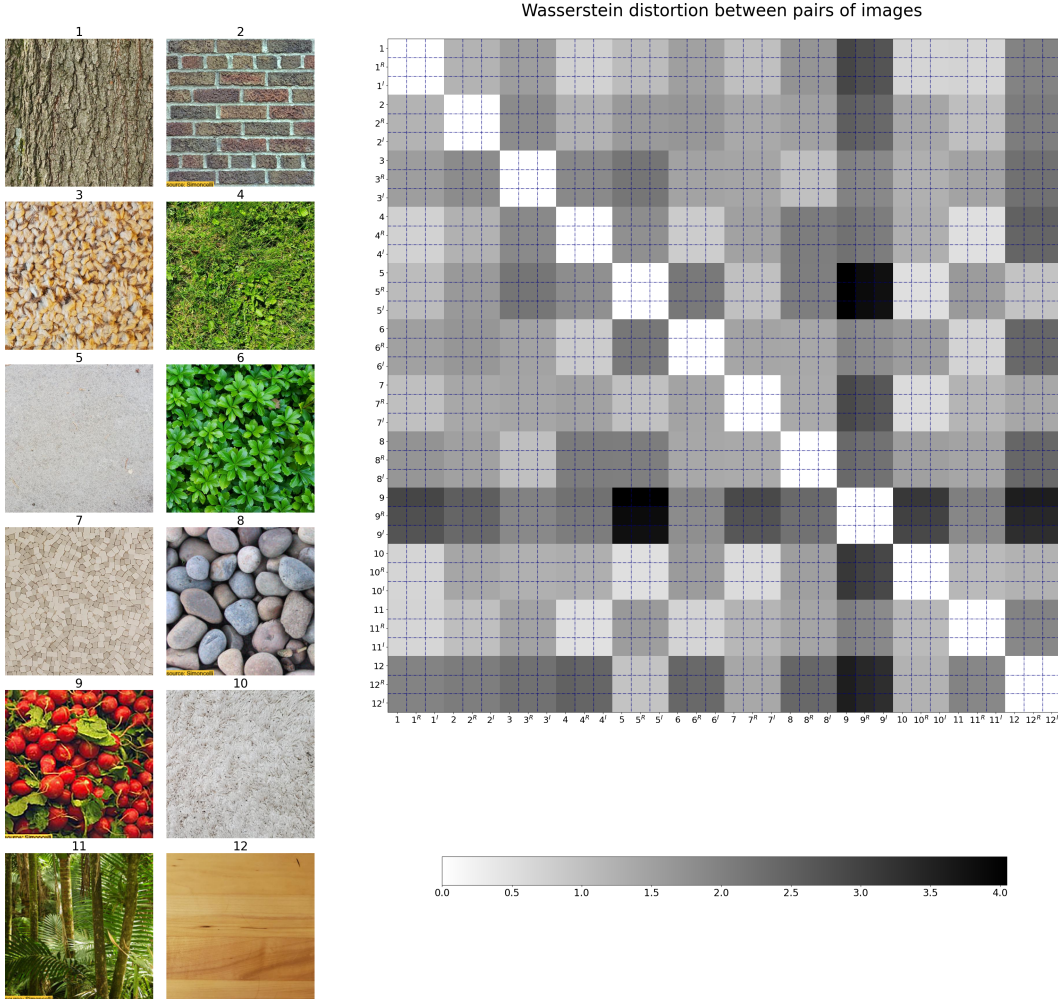


Figure 10: Wasserstein distortion between pairs of images from Experiments 1 and 2, normalized by the number of features and number of pixels of interest. Each number refers to one reference texture; number^R refers to the corresponding pinned reproduction texture (see column 4 of Fig. 4 and Fig. 5), and number^I refers to the corresponding independent reproduction texture (see column 2 of Fig. 4 and Fig. 5). We see that the Wasserstein distortion between images of the same texture are small compared with the Wasserstein distortion between different textures.

REFERENCES

- Eirikur Agustsson, Michael Tschannen, Fabian Mentzer, Radu Timofte, and Luc Van Gool. Generative adversarial networks for extreme image compression. In *Proceedings of the IEEE/CVF International Conference on Computer Vision*, pp. 221–231, 2019. doi: 10.1109/iccv.2019.00031.
- İsmail Avcıbaşı, Bülent Sankur, and Khalid Sayood. Statistical evaluation of image quality measures. *Journal of Electronic Imaging*, 11(2):206–223, 2002. doi: 10.1117/1.1455011.
- Benjamin Balas, Lisa Nakano, and Ruth Rosenholtz. A summary-statistic representation in peripheral vision explains visual crowding. *Journal of Vision*, 9(12):13–13, 2009. doi: 10.1167/9.12.13.
- Toby Berger. *Rate Distortion Theory: A Mathematical Basis for Data Compression*. Prentice-Hall, Inc., 1971. doi: 10.1002/0471219282.eot142.
- Yochai Blau and Tomer Michaeli. The perception-distortion tradeoff. In *Proceedings of the IEEE Conference on Computer Vision and Pattern Recognition*, pp. 6228–6237, 2018. doi: 10.1109/cvpr.2018.00652.
- Yochai Blau and Tomer Michaeli. Rethinking lossy compression: The rate-distortion-perception tradeoff. In *Proceedings of the 36th International Conference on Machine Learning*, pp. 675–685. PMLR, 09–15 Jun 2019. URL <https://proceedings.mlr.press/v97/blau19a.html>.
- Nicolas Bonneel, Julien Rabin, Gabriel Peyré, and Hanspeter Pfister. Sliced and Radon Wasserstein barycenters of measures. *Journal of Mathematical Imaging and Vision*, 51:22–45, 2015. doi: 10.1007/s10851-014-0506-3.
- Antoni Buades, Bartomeu Coll, and Jean-Michel Morel. A review of image denoising algorithms, with a new one. *Multiscale Modeling & Simulation*, 4(2):490–530, 2005. doi: 10.1137/040616024.
- Jun Chen, Lei Yu, Jia Wang, Wuxian Shi, Yiqun Ge, and Wen Tong. On the rate-distortion-perception function. *IEEE Journal on Selected Areas in Information Theory*, 2022. doi: 10.1109/JSAIT.2022.3231820.
- Kejiang Chen, Hang Zhou, Hanqing Zhao, Dongdong Chen, Weiming Zhang, and Nenghai Yu. Distribution-preserving steganography based on text-to-speech generative models. *IEEE Transactions on Dependable and Secure Computing*, 19(5):3343–3356, 2021. doi: 10.1109/TDSC.2021.3095072.
- Marco Cuturi. Sinkhorn distances: Lightspeed computation of optimal transport. *Advances in Neural Information Processing Systems*, 26, 2013. URL <https://proceedings.neurips.cc/paper/2013/hash/af21d0c97db2e27e13572cbf59eb343d-Abstract.html>.
- Edward J. Delp and O. Robert Mitchell. Moment preserving quantization (signal processing). *IEEE Transactions on Communications*, 39(11):1549–1558, 1991. doi: 10.1109/26.111432.
- Jia Deng, Wei Dong, Richard Socher, Li-Jia Li, Kai Li, and Li Fei-Fei. Imagenet: A large-scale hierarchical image database. In *2009 IEEE Conference on Computer Vision and Pattern Recognition*, pp. 248–255. IEEE, 2009. doi: 10.1109/cvpr.2009.5206848.
- Richard Dosselmann and Xue Dong Yang. Existing and emerging image quality metrics. In *Canadian Conference on Electrical and Computer Engineering, 2005.*, pp. 1906–1913. IEEE, 2005. doi: 10.1109/CCECE.2005.1557355.
- Serge O. Dumoulin and Brian A. Wandell. Population receptive field estimates in human visual cortex. *Neuroimage*, 39(2):647–660, 2008. doi: 10.1016/j.neuroimage.2007.09.034.
- Richard Durrett. *Probability: Theory and Examples*. Duxbury Press, 2nd edition, 1996. ISBN 978-0-521-76539-8. doi: 10.5555/1869916.

-
- Ariel Elnekave and Yair Weiss. Generating natural images with direct patch distributions matching. In *Computer Vision – ECCV 2022*, pp. 544–560, 2022. doi: 10.1007/978-3-031-19790-1_33.
- Jiaojiao Fan, Shu Liu, Shaojun Ma, Yongxin Chen, and Hao-Min Zhou. Scalable computation of monge maps with general costs. In *ICLR Workshop on Deep Generative Models for Highly Structured Data*, 2022. URL <https://openreview.net/forum?id=rEnGR3VdDW5>.
- Jeremy Freeman and Eero P. Simoncelli. Metamers of the ventral stream. *Nature Neuroscience*, 14(9):1195–1201, 2011. doi: 10.1038/nn.2889.
- S. Gao, Y. Shi, T. Guo, Z. Qiu, Y. Ge, Z. Cui, Y. Feng, J. Wang, and B. Bai. Perceptual learned image compression with continuous rate adaptation. In *4th Challenge on Learned Image Compression*, Jun 2021.
- Leon Gatys, Alexander S. Ecker, and Matthias Bethge. Texture synthesis using convolutional neural networks. *Advances in Neural Information Processing Systems*, 28, 2015. URL https://proceedings.neurips.cc/paper_files/paper/2015/file/a5e00132373a7031000fd987a3c9f87b-Paper.pdf.
- Nicolas Gonthier, Yann Gousseau, and Saïd Ladjal. High-resolution neural texture synthesis with long-range constraints. *Journal of Mathematical Imaging and Vision*, 64(5):478–492, 2022. doi: 10.1007/s10851-022-01078-y.
- Yassine Hamdi and Deniz Gündüz. The rate-distortion-perception trade-off with side information. *arXiv preprint arXiv:2305.13116*, 2023. doi: 10.48550/arXiv.2305.13116.
- Eric Heitz, Kenneth Vanhoey, Thomas Chambon, and Laurent Belcour. A sliced Wasserstein loss for neural texture synthesis. In *Proceedings of the IEEE/CVF Conference on Computer Vision and Pattern Recognition (CVPR)*, pp. 9412–9420, June 2021. doi: 10.1109/cvpr46437.2021.00929.
- Martin Heusel, Hubert Ramsauer, Thomas Unterthiner, Bernhard Nessler, and Sepp Hochreiter. Gans trained by a two time-scale update rule converge to a local nash equilibrium. *Advances in Neural Information Processing Systems*, 30, 2017. URL https://proceedings.neurips.cc/paper_files/paper/2017/file/8ald694707eb0fefe65871369074926d-Paper.pdf.
- Alain Hore and Djemel Ziou. Image quality metrics: Psnr vs. ssim. In *2010 20th International Conference on Pattern Recognition*, pp. 2366–2369. IEEE, 2010. doi: 10.1109/ICPR.2010.579.
- Antoine Houdard, Arthur Leclaire, Nicolas Papadakis, and Julien Rabin. A generative model for texture synthesis based on optimal transport between feature distributions. *Journal of Mathematical Imaging and Vision*, 65:4–28, 2023. doi: 10.1007/s10851-022-01108-9.
- Ming Jiang, Shengsheng Huang, Juanyong Duan, and Qi Zhao. Salicon: Saliency in context. In *Proceedings of the IEEE Conference on Computer Vision and Pattern Recognition*, pp. 1072–1080, 2015. doi: 10.1109/cvpr.2015.7298710.
- Janusz Klejsa, Guoqiang Zhang, Minyue Li, and W. Bastiaan Kleijn. Multiple description distribution preserving quantization. *IEEE Transactions on Signal Processing*, 61(24):6410–6422, 2013. doi: 10.1109/TSP.2013.2286773.
- Younghee Kwon, Kwang In Kim, James Tompkin, Jin Hyung Kim, and Christian Theobalt. Efficient learning of image super-resolution and compression artifact removal with semi-local Gaussian processes. *IEEE Transactions on Pattern Analysis and Machine Intelligence*, 37(9):1792–1805, 2015. doi: 10.1109/TPAMI.2015.2389797.
- Chun-Liang Li, Wei-Cheng Chang, Yu Cheng, Yiming Yang, and Barnabás Póczos. Mmd gan: Towards deeper understanding of moment matching network. *Advances in Neural Information Processing Systems*, 30, 2017. URL https://proceedings.neurips.cc/paper_files/paper/2017/file/dfd7468ac613286cddb40872c8ef3b06-Paper.pdf.

-
- Chun-Liang Li, Wei-Cheng Chang, Youssef Mroueh, Yiming Yang, and Barnabas Poczos. Implicit kernel learning. In *The 22nd International Conference on Artificial Intelligence and Statistics*, pp. 2007–2016. PMLR, 16–18 Apr 2019. URL <https://proceedings.mlr.press/v89/li19f.html>.
- Minyue Li, Janusz Klejsa, and W. Bastiaan Kleijn. On distribution preserving quantization. QC 20110829, 2011.
- Bingchen Liu, Yizhe Zhu, Kunpeng Song, and Ahmed Elgammal. Towards faster and stabilized {gan} training for high-fidelity few-shot image synthesis. In *International Conference on Learning Representations*, 2020. URL <https://openreview.net/forum?id=1Fqg133qRaI>.
- Gang Liu, Yann Gousseau, and Gui-Song Xia. Texture synthesis through convolutional neural networks and spectrum constraints. In *2016 23rd International Conference on Pattern Recognition (ICPR)*, pp. 3234–3239, 2016. doi: 10.1109/ICPR.2016.7900133.
- Mario Lucic, Karol Kurach, Marcin Michalski, Sylvain Gelly, and Olivier Bousquet. Are gans created equal? a large-scale study. *Advances in Neural Information Processing Systems*, 31, 2018. URL https://proceedings.neurips.cc/paper_files/paper/2018/file/e46de7e1bcaaced9a54f1e9d0d2f800d-Paper.pdf.
- Ryutaroh Matsumoto. Introducing the perception-distortion tradeoff into the rate-distortion theory of general information sources. *IEICE Communications Express*, 7(11):427–431, 2018. doi: 10.1587/comex.2018XBL0109.
- Ryutaroh Matsumoto. Rate-distortion-perception tradeoff of variable-length source coding for general information sources. *IEICE Communications Express*, 8(2):38–42, 2019. doi: 10.1587/comex.2018XBL0139.
- Fabian Mentzer, George D Toderici, Michael Tschannen, and Eirikur Agustsson. High-fidelity generative image compression. *Advances in Neural Information Processing Systems*, 33:11913–11924, 2020. URL https://proceedings.neurips.cc/paper_files/paper/2020/file/8a50bae297807da9e97722a0b3fd8f27-Paper.pdf.
- Seungjun Nah, Sanghyun Son, Suyoung Lee, Radu Timofte, and Kyoung Mu Lee. Ntire 2021 challenge on image deblurring. In *Proceedings of the IEEE/CVF Conference on Computer Vision and Pattern Recognition*, pp. 149–165, 2021. doi: 10.1109/cvprw.2019.00251.
- Xueyan Niu, Deniz Gündüz, Bo Bai, and Wei Han. Conditional rate-distortion-perception trade-off. *arXiv preprint arXiv:2305.09318*, 2023. doi: 10.48550/arXiv.2305.09318.
- I. Olkin and F. Pukelsheim. The distance between two random vectors with given dispersion matrices. *Linear Algebra and its Applications*, 48:257–263, 1982. doi: 10.1016/0024-3795(82)90112-4.
- William A. Pearlman and Amir Said. *Digital Signal Compression: Principles and Practice*. Cambridge university press, 2011. ISBN 978-0-521-89982-6. doi: 10.1017/CBO9780511984655.
- F. Pitié, A.C. Kokaram, and R. Dahyot. n -dimensional probability density function transfer and its application to color transfer. In *Tenth IEEE International Conference on Computer Vision (ICCV’05) Volume 1*, volume 2, pp. 1434–1439, 2005. doi: 10.1109/ICCV.2005.166.
- Javier Portilla and Eero P. Simoncelli. A parametric texture model based on joint statistics of complex wavelet coefficients. *International Journal of Computer Vision*, 40:49–70, 2000. doi: 10.1023/A:1026553619983.
- Oren Rippel and Lubomir Bourdev. Real-time adaptive image compression. In *International Conference on Machine Learning*, pp. 2922–2930. PMLR, 06–11 Aug 2017. URL <https://proceedings.mlr.press/v70/rippel17a.html>.
- Ruth Rosenholtz. What your visual system sees where you are not looking. In *Human Vision and Electronic Imaging XVI*, volume 7865, pp. 343–356. SPIE, 2011. doi: 10.1117/12.876659.

-
- Ruth Rosenholtz, Jie Huang, Alvin Raj, Benjamin J Balas, and Livia Ilie. A summary statistic representation in peripheral vision explains visual search. *Journal of Vision*, 12(4):14–14, 2012. doi: 10.1167/12.4.14.
- Yossi Rubner, Carlo Tomasi, and Leonidis J. Guibas. The earth mover’s distance as a metric for image retrieval. *International Journal of Computer Vision*, 40(2):99–121, 2000. doi: 10.1023/A:1026543900054.
- Naci Saldi, Tamás Linder, and Serdar Yüksel. Randomized quantization and source coding with constrained output distribution. *IEEE Transactions on Information Theory*, 61(1):91–106, 2014. doi: 10.1109/TIT.2014.2373382.
- Sadaf Salehkalaibar, Buu Phan, Ashish Khisti, and Wei Yu. Rate-distortion-perception tradeoff based on the conditional perception measure. In *2023 Biennial Symposium on Communications (BSC)*, pp. 31–37. IEEE, 2023. doi: 10.1109/BSC57238.2023.10201822.
- Khalid Sayood. *Introduction to Data Compression*. Morgan Kaufmann, 2017. ISBN 978-1-55860-558-9. doi: 10.1016/B978-0-12-620862-7.X5000-7.
- Omry Sendik and Daniel Cohen-Or. Deep correlations for texture synthesis. *ACM Transactions on Graphics (ToG)*, 36(5):1–15, 2017. doi: 10.1145/3015461.
- Eero P. Simoncelli and William T. Freeman. The steerable pyramid: A flexible architecture for multi-scale derivative computation. In *Proceedings., International Conference on Image Processing*, volume 3, pp. 444–447 vol.3, 1995. doi: 10.1109/ICIP.1995.537667.
- Karen Simonyan and Andrew Zisserman. Very deep convolutional networks for large-scale image recognition. In *3rd International Conference on Learning Representations (ICLR 2015)*. Computational and Biological Learning Society, 2015. URL <https://doi.org/10.48550/arXiv.1409.1556>.
- Alexander J. Smola, A. Gretton, and K. Borgwardt. Maximum mean discrepancy. In *13th International Conference, ICONIP*, pp. 3–6, 2006.
- Xavier Snelgrove. High-resolution multi-scale neural texture synthesis. In *SIGGRAPH Asia 2017 Technical Briefs*, 2017. doi: 10.1145/3145749.3149449.
- Guillaume Tartavel, Gabriel Peyré, and Yann Gousseau. Wasserstein loss for image synthesis and restoration. *SIAM Journal on Imaging Sciences*, 9(4):1726–1755, 2016. doi: 10.1137/16M1067494.
- Lucas Theis and Aaron B. Wagner. A coding theorem for the rate-distortion-perception function. In *Neural Compression: From Information Theory to Applications – Workshop @ ICLR 2021*, 2021. URL <https://openreview.net/forum?id=BzUaLGtKecs>.
- Lucas Theis, Tim Salimans, Matthew D. Hoffman, and Fabian Mentzer. Lossy compression with Gaussian diffusion. *arXiv preprint arXiv:2206.08889*, 2022. doi: 10.48550/arXiv.2206.08889.
- Michael Tschannen, Eirikur Agustsson, and Mario Lucic. Deep generative models for distribution-preserving lossy compression. *Advances in Neural Information Processing Systems*, 31, 2018. URL https://proceedings.neurips.cc/paper_files/paper/2018/file/801fd8c2a4e79c1d24a40dc735c051ae-Paper.pdf.
- Ivan Ustyuzhaninov, Wieland Brendel, Leon Gatys, and Matthias Bethge. What does it take to generate natural textures? In *International Conference on Learning Representations*, 2017. URL <https://openreview.net/forum?id=BJhZeLsxx>.
- Cédric Villani. *Optimal Transport: Old and New*, volume 338. Springer, 2009. doi: 10.1007/978-3-540-71050-9.
- Aaron B. Wagner. The rate-distortion-perception tradeoff: The role of common randomness. *arXiv preprint arXiv:2202.04147*, 2022. doi: 10.48550/arXiv.2202.04147.

-
- Xintao Wang, Ke Yu, Shixiang Wu, Jinjin Gu, Yihao Liu, Chao Dong, Yu Qiao, and Chen Change Loy. Esrgan: Enhanced super-resolution generative adversarial networks. In *Proceedings of the European Conference on Computer Vision (ECCV) Workshops*, pp. 0–0, 2018. doi: 10.1007/978-3-030-11021-5_5.
- Zhou Wang and Alan C Bovik. Mean squared error: Love it or leave it? a new look at signal fidelity measures. *IEEE Signal Processing Magazine*, 26(1):98–117, 2009. doi: 10.1109/MSP.2008.930649.
- Zhou Wang, Alan C. Bovik, Hamid R. Sheikh, and Eero P. Simoncelli. Image quality assessment: From error visibility to structural similarity. *IEEE Transactions on Image Processing*, 13(4): 600–612, 2004. doi: 10.1109/TIP.2003.819861.
- George Zhang, Jingjing Qian, Jun Chen, and Ashish Khisti. Universal rate-distortion-perception representations for lossy compression. *Advances in Neural Information Processing Systems*, 34:11517–11529, 2021. URL https://proceedings.neurips.cc/paper_files/paper/2021/file/5fde40544cff0001484ecae2466ce96e-Paper.pdf.
- Yang Zhou, Zhen Zhu, Xiang Bai, Dani Lischinski, Daniel Cohen-Or, and Hui Huang. Non-stationary texture synthesis by adversarial expansion. *ACM Transactions on Graphics (ToG)*, 37(4), Jul 2018. doi: 10.1145/3197517.3201285.
- Ciyu Zhu, Richard H. Byrd, Peihuang Lu, and Jorge Nocedal. Algorithm 778: L-bfgs-b: Fortran subroutines for large-scale bound-constrained optimization. *ACM Transactions on Mathematical Software (TOMS)*, 23(4):550–560, 1997. doi: 10.1145/279232.279236.